Synthetic Aperture Fourier Holographic Optical Microscopy

Sergey A. Alexandrov,* Timothy R. Hillman, Thomas Gutzler, and David D. Sampson

Optical+Biomedical Engineering Laboratory, School of Electrical, Electronic and Computer Engineering, The University of Western Australia, Crawley, WA, 6009, Australia

(Received 6 April 2006; published 18 October 2006)

We report a new synthetic aperture optical microscopy in which high-resolution, wide-field amplitude and phase images are synthesized from a set of Fourier holograms. Each hologram records a region of the complex two-dimensional spatial frequency spectrum of an object, determined by the illumination field's spatial and spectral properties and the collection angle and solid angle. We demonstrate synthetic microscopic imaging in which spatial frequencies that are well outside the modulation transfer function of the collection optical system are recorded while maintaining the long working distance and wide field of view.

DOI: 10.1103/PhysRevLett.97.168102 PACS numbers: 87.64.Rr, 42.40.−i, 42.30.Kq, 42.30.Lr

Optical microscopy is one of the most extensively used tools in the life and material sciences. To achieve the highest resolutions, sophisticated high-numerical-aperture (NA) objective lenses have been realized. Alternative pathways to subwavelength resolution based on near-field [1–3] and far-field [4,5] techniques have also been developed. A high-NA lens brings with it constraints on the field of view and the working distance that are limitations in many applications. A field of view smaller than the region of interest is usually dealt with by moving the sample or objective to record multiple tiled images. Here, we present an alternative procedure, drawing together three innovations in classical optics to relax the constraints on the optical components, thereby allowing greatly increased working distance, field of view, and contrast of the highest spatial frequencies. The first of these innovations is Zernike's phase contrast microscope [6,7], which transformed the microscopic visualization of phase objects. The second is Gabor's invention, holography [8], and its relatively recent application to phase (and amplitude) microscopic imaging [9–11]. The final innovation is Ryle's concept of the synthetic aperture, first applied to increase the resolution of the radio telescope [12] and later to synthetic aperture radar [13]. We report their combination in a new synthetic aperture phase and amplitude microscopy based on Fourier holography.

There have been previous attempts to apply the principle of the synthetic aperture to optical imaging [14–19], with the objective of enhancing resolution, as well as the modulation transfer function (MTF) [14], depth of focus, field of view, and working distance [19]. Several of these concerned microscopy [14,19] and have employed holography [15–18] or interferometry [19]. Innovations have included off-axis illumination [14,16,18,19], Fourier plane synthesis [15,16], and extended recording planes [17]. Improvements in resolution and other quantities have been demonstrated, but there is no effective method of synthesizing the complex amplitude of a sample wave over both a large range of spatial frequencies and a wide field of view simultaneously. In this Letter, we introduce and demonstrate synthetic aperture Fourier holographic microscopy, in which amplitude and phase images are synthesized from a set of digital holograms of different regions of the two-dimensional complex spatial Fourier spectrum of a wave after interaction with a sample. Selection of an area of the Fourier spectrum is performed via control of the angular and/or spectral properties of the illumination and collection light fields. We show high-synthetic-NA images containing spatial frequencies that are well outside the MTF of the long working distance, low-NA collection optical system, while maintaining its wide field of view.

The principle of synthetic aperture Fourier holography is illustrated in Fig. 1. A sample is located in the object plane, with coordinates ξ, η, and a recording is performed in the recording plane, with coordinates x, y, optically conjugate to the back focal (Fourier) plane of the objective. Let $r(\xi, \eta)$ be the complex scalar reflectance or transmission profile of the sample, and the illumination wave be plane and have polar angle θ_i and azimuthal angle ϕ_i, as shown. The complex scalar field of the reflected or transmitted wave (sample wave) in the object plane is given by $U_i(\xi, \eta) = r(\xi, \eta)A_i(\xi, \eta)$, where $A_i(\xi, \eta) = A_0 \exp[-j2\pi(\gamma_\xi \xi + \gamma_\eta \eta)]$ is the complex scalar field of the illumination wave in the object plane. The quantity A_0 is a complex constant and γ_ξ, γ_η represent the illumination wave spatial frequencies in the object plane, so that, for wavelength λ, $\lambda\gamma_\xi = \sin\theta_i \cos\phi_i$, and $\lambda\gamma_\eta = \sin\theta_i \sin\phi_i$. The complex scalar field in the recording plane $U_S(x, y)$, the scaled and phase-shifted Fourier transform of $U_i(\xi, \eta)$, is recorded holographically. The sample spatial frequency magnitude ν_s that yields diffraction or scattering into the angle α_{out} in the plane of incidence [as shown in Fig. 1(b)] can be written as [20]

$$\nu_s = \frac{|\sin\theta_i - \sin\alpha_{\text{out}}|}{\lambda}. \quad (1)$$

Off-axis holography is performed by using a plane reference beam [Fig. 1(a)], with polar angle θ_r and azimuthal angle ϕ_r, and complex scalar field denoted $U_R(x, y)$. The recording area, assumed rectangular, is given by $-L/2 \le x \le L/2$, $-H/2 \le y \le H/2$, where L, H are, respec-

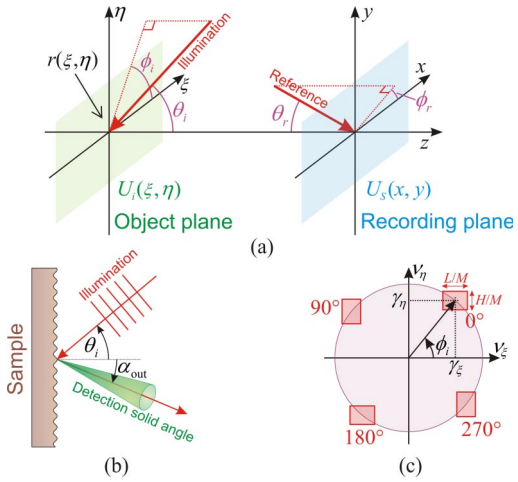

FIG. 1 (color online). (a) Orientation of object (sample) and recording (Fourier) planes, and illumination and reference waves, with respect to the optical axis z; (b) depiction of the incident and scattered or diffracted waves in the plane of incidence, and the collection solid angle; (c) range of spatial frequencies covered in four separate holographic recordings (labeled 0°, 90°, 180°, and 270°). The range covered by a single 0.75 NA lens (for a coherent imaging system) is also shown.

tively, the length and height of the detector array (hereafter, "detector"). The recorded intensity image is

$$I_H(x, y) = |U_S(x, y) + U_R(x, y)|^2 \mathrm{rect}\left(\frac{x}{L}, \frac{y}{H}\right). \quad (2)$$

When inverse Fourier transformed, the image comprises zero-order autocorrelation and background images, and translated twin conjugate complex reconstructions of the sample field (over the range of spatial frequencies captured). As demonstrated in Eq. (1), the use of an off-axis illumination beam ensures that a nonzero sample spatial frequency gives rise to the on-axis diffracted beam ($\alpha_{\text{out}} = 0$). The range of diffraction angles captured by the detector, centered on the axis, corresponds to the following range of sample spatial frequencies (in the ξ, η directions, respectively):

$$\nu_{\xi,\min/\max} = \mp\frac{L}{2M} + \gamma_\xi, \qquad \nu_{\eta,\min/\max} = \mp\frac{H}{2M} + \gamma_\eta, \quad (3)$$

where M is a constant dependent on the collection system, and directly proportional to λ. Equation (1) shows that it is possible to vary the sample spatial frequencies captured by varying the parameters of both the incident and diffracted waves, specifically their angles and/or wavelength. Equation (3) gives the range of recorded spatial frequencies for a given incident angle, assuming the collection solid angle is limited by the size of the detector. If the detector is not restricted to the on-axis location, Eq. (3) is not applicable, and higher spatial frequencies could be recorded according to Eq. (1). In the limiting case of $\theta_i = 90°$ and $\alpha_{\text{out}} = -90°$, the spatial frequency limit is $\nu_s = 2/\lambda$, which is twice the theoretical cutoff spatial frequency of conventional coherent imaging systems and the equal of incoherent systems (without immersion). Moreover, our approach has a dramatically improved spatial frequency response when compared to the MTF of conventional microscopy using incoherent illumination, in theory maintaining the high contrast of coherent illumination up to the cutoff frequency.

To yield the synthetic image, we firstly reconstructed the complex sample field from each individual Fourier hologram, by inverse Fourier-transforming $I_H(x, y)$. The resulting array was translated by an amount determined by the reference beam off-axis angle, and postmultiplied by a carrier function with spatial frequency (γ_ξ, γ_η), resulting in a reconstruction of $r(\xi, \eta)$ over the frequency range represented by Eq. (3). The fact that the hologram was recorded digitally also allowed for the numerical correction of defocusing in both the object and recording plane. The synthesized image was then obtained by summing the resulting complex fields of the sample $r(\xi, \eta)$ over the different spatial frequency ranges represented by the multiple recordings. Any area of the image could be selected to perform this operation.

The technique can be applied to scattering, diffracting, and pure phase objects, in both transmission and reflection. We used a reflection configuration in experiments, as shown in Fig. 1(b), to enable the study of thick and nontransparent samples [21]. The illumination source was a red helium-neon laser. Light collected by the objective lens (focal length 15 mm, working distance 13 mm) was magnified and recorded using a charge-coupled device (CCD) (1392 × 1040 pixels) located in a plane conjugate to the Fourier plane of the objective. The collection solid angle of the setup is equivalent to an NA of 0.13. As shown in Fig. 1(a), the optical axis of the collected beam was perpendicular to the surface of the sample ($\alpha_{\text{out}} = 0$), thus, Eq. (3) applies. To change the azimuthal incident angle and, therefore, the location in the Fourier plane accessed by the hologram, samples were rotated around the optical axis.

We recorded four Fourier holograms with azimuthal angles at 90° intervals, covering the regions of the spatial frequency spectrum shown in Fig. 1(c). As suggested by the figure, the four regions were identified with the azimuthal angles 0°, 90°, 180°, and 270°. The field of view on the sample was approximately 1 × 1 mm. Two samples containing microstructures significantly smaller than the resolution limit of the collection optics were chosen. The first sample was a ruled reflection diffraction grating of 1200 lines/mm (The Optometrics Group). The second sample was a transmission electron microscopy calibration grid target (Ladd Research Industries Inc.) consisting of a germanium-shadowed carbon replica made from a 28 800 lines/in diffraction grating mounted on a grid with 125 μm pitch, 97 μm holes, and 28 μm bars. This target produces diffraction from the grating structure and

wide-band scattering from the grid structure. Both samples were oriented so that the first-order diffraction spots associated with the gratings were imaged at azimuthal angles 0° and 180°.

Figure 2(a) shows the full-sized amplitude image of the first sample reconstructed from a single hologram recorded using an incident azimuthal angle of 0° and a polar angle of 49°, the latter corresponding to a synthetic NA of 0.76. Figures 2(b) and 2(c) present phase images of selected, successively magnified areas of the image synthesized using the four holograms. The dark and light lines on the synthesized images correspond to the lines on the grating. For comparison, Fig. 2(d) shows a confocal reflectance image of the grating obtained using an oil immersion objective lens (NA = 1.0).

Synthetic imaging of the second, more complex sample is demonstrated in Fig. 3. Figure 3(a) shows a confocal reflectance image of a large portion of the target (10× objective lens) and Fig. 3(b) shows a differential interference contrast (DIC) image (40× objective lens, NA = 0.75) showing the substructure, including a strip processed using an edge-detecting filter to enhance the contrast. For synthetic imaging, an incident polar angle of 46°, corresponding to a synthetic NA of 0.72, was used. Reconstructed full-size images for azimuthal angles of 0° and 90° are shown in Figs. 3(c) and 3(d). Figure 3(e) shows an image corresponding to the highlighted region in Figs. 3(c) and 3(d), synthesized from azimuthal angles 90° and 270°. This image was formed from waves scattered from the grid structure, since diffracted waves were absent at those angles and, as a result, it is dominated by speckle. Figure 3(f) shows the synthetic image incorporating all azimuthal angles. Amplitude and phase images of the highlighted regions of Fig. 3(f) are shown in Figs. 3(g)–3(j), respectively. The difference between the scattering grid structure and the diffracting fine grating structure is marked. The scattering structure contains spatial frequency components in two distinct orientations, determined by the four azimuthal angle positions, whereas, the diffracting structure is dominated by a single spatial frequency, oriented according to the grating direction. Increasing the number of holograms used to synthesize the image would lead to additional spatial frequency components in different directions being incorporated into

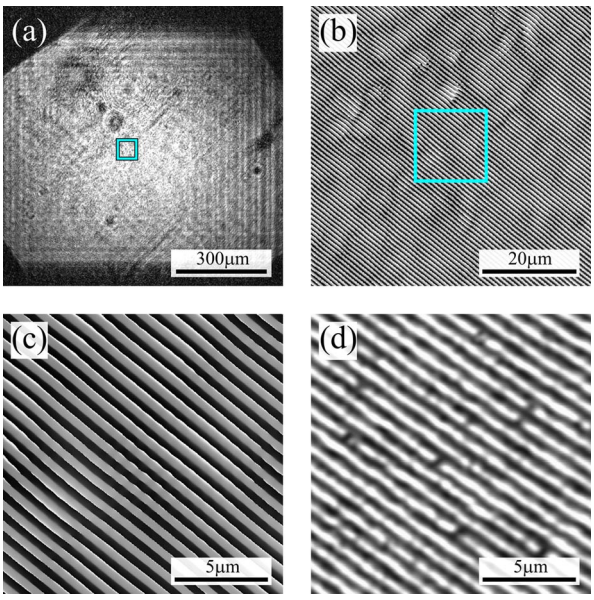

FIG. 2 (color online). Images of a ruled reflection grating of 1200 lines/mm: (a) Reconstructed full-size image for azimuthal angle 0°; (b), (c) phase images of selected and successively enlarged areas of synthesized image; (d) confocal microscope image.

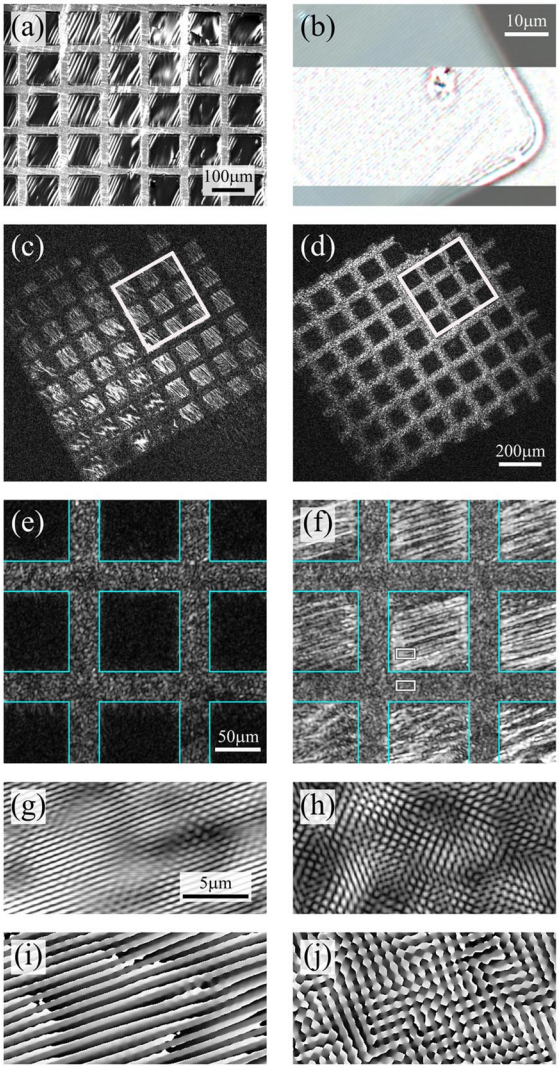

FIG. 3 (color online). Images of a grid target: (a) Confocal; (b) DIC; (c), (d) reconstructed full-size images for azimuthal angles 0° and 90° [scale bar in (d)]; (e) Synthetic image using 90° and 270° azimuthal angles; (f) Synthetic image using all azimuthal angles [scale bar in (e)]—grid lines are a guide to the eye; (g), (h) Magnified amplitude images of upper/lower highlighted regions of (f), respectively, [scale bar in (g)]; (i), (j) Magnified phase images of highlighted regions of (f) [scale bar in (g)].

Figs. 3(h) and 3(j), whereas Figs. 3(g) and 3(i) would remain essentially unchanged. As a result, chaotic structure would be observed in the grid image, but regular structure maintained in the grating image.

The reconstructed images in Figs. 2 and 3 display the submicron-period structures (0.83 and 0.88 μm, respectively) with high contrast over a 1×1 mm field of view, and validate the concept. The ruled lines of the 1200 lines/mm grating are clearly resolved in Fig. 2(c), although the maximum spatial frequency of the theoretical MTF of the objective lens is 400 lines/mm. Since probing such high spatial frequencies depends on the illumination or collection angles and not on the collection solid angle, higher resolution than demonstrated here over much larger samples should be feasible. The choice of collection solid angle represents a trade off between the number of holograms to be recorded and the working distance or detector size.

In contrast to other methods [19], holographic recording in the Fourier plane enables both amplitude and phase imaging to be performed with greatly relaxed constraints on the field of view for a given number of available detector pixels. As mentioned above, recording close to on-axis diffraction leads to a coherent transfer function over the synthetic aperture that can be controlled and greatly enhanced at high spatial frequencies relative to the MTF of an objective of the same NA [14]. The enhanced spatial frequency response is in evidence in comparing the contrast in Fig. 3(b) (NA = 0.75) and Fig. 3(g) (synthetic NA = 0.72); in Fig. 3(b) the contrast of the microstructure is low because its frequency is close to cutoff.

To correctly synthesize the complex Fourier field from the set of recorded holograms, it is necessary in general to correctly set the relative amplitude and phase factors between the separately recorded complex amplitudes. Uncontrolled phase factors in our experiments did not affect the quality of the reconstructed images because the high-spatial frequency components of our samples consisted of the special case of uniform grating structures. Phases may be controlled interferometrically during adjustment of the incident wave, or inferred from partially overlapping Fourier holograms [15,16,18] or *a priori* sample knowledge. The system is intrinsically tolerant to lateral object translations (which may occur, for example, if the object rotation and collection optical axes do not coincide). Such translations contribute only a linear phase ramp to the field distribution in the Fourier plane, but all Fourier components will remain in the same positions. Misalignments of the setup during reconstruction can be corrected by using a reference object with known structure for calibration.

Numerical synthesis of the whole Fourier spectrum of a sample would make it possible to form an image with unique properties which endow our technique with several advantages over existing microscopic techniques. The synthetic image has a spatial resolution set by its synthetic NA, which would otherwise require use of an immersion objective or similar high-NA lens, but preserves the large field of view (and long working distance) of the low-NA collection optics. Selective recording of spatial frequencies could be used to efficiently image certain features of a sample, for example, microstructures of a given size. Since we record the full complex amplitude of the object wave, our technique is well suited to performing phase imaging. Another interesting application of this approach could be high-resolution imaging of three-dimensional objects, especially those with significant height variations over the region of interest. Synthetic aperture Fourier holographic microscopy promises wide application in medicine, biology, and the material sciences.

S. A. A. is supported by the Raine Medical Research Foundation.

*Electronic address: sergey@ee.uwa.edu.au

[1] E. Betzig and J. K. Trautman, Science **257**, 189 (1992).
[2] R. C. Reddick, R. J. Warmack, and T. L. Ferrell, Phys. Rev. B **39**, 767 (1989).
[3] T. Kalkbrenner, U. Håkanson, A. Schädle, S. Burger, C. Henkel, and V. Sandoghdar, Phys. Rev. Lett. **95**, 200801(2005).
[4] I. I. Smolyaninov, J. Elliott, A. V. Zayats, and C. C. Davis, Phys. Rev. Lett. **94**, 057401 (2005).
[5] E. Baleine and A. Dogariu, Phys. Rev. Lett. **95**, 193904 (2005).
[6] F. Zernike, Physica (Amsterdam) **9**, 686 (1942).
[7] F. Zernike, Physica (Amsterdam) **9**, 974 (1942).
[8] D. Gabor, Nature (London) **161**, 777 (1948).
[9] C. J. Mann, L. Yu, C.-M. Lo, and M. K. Kim, Opt. Express **13**, 8693 (2005).
[10] M. Sebesta and M. Gustafsson, Opt. Lett. **30**, 471 (2005).
[11] B. Rappaz, P. Marquet, E. Cuche, Y. Emery, C. Depeursinge, and P. J. Magistretti, Opt. Express **13**, 9361 (2005).
[12] M. Ryle and A. Hewish, Mon. Not. R. Astron. Soc. **120**, 220 (1960).
[13] C. Oliver and S. Quegan, *Understanding Synthetic Aperture Radar Images* (Artech House, Boston, 1998).
[14] H. Dupoisot, A. Poletaeff, G. Daury, and P. de Vernejoul, Opt. Commun. **72**, 42 (1989).
[15] F. Le Clerc, M. Gross, and L. Collot, Opt. Lett. **26**, 1550 (2001).
[16] J. H. Massig, Opt. Lett. **27**, 2179 (2002).
[17] T. Kreis, M. Adams, and W. Jüptner, Proc. SPIE-Int. Soc. Opt. Eng. **4777**, 69 (2002).
[18] R. Binet, J. Colineau, and J.-C. Lehureau, Appl. Opt. **41**, 4775 (2002).
[19] C. J. Schwarz, Y. Kuznetsova, and S. R. J. Brueck, Opt. Lett. **28**, 1424 (2003).
[20] S. A. Alexandrov, T. R. Hillman, T. Gutzler, M. B. Same, and D. D. Sampson, Proc. SPIE-Int. Soc. Opt. Eng. **6081**, 15 (2006).
[21] S. A. Alexandrov, T. R. Hillman, and D. D. Sampson, Opt. Lett. **30**, 3305 (2005).